

VIS-Magneto-optical spectroscopy of ferromagnetic garnet thin films

Marina Espínola Seral

Facultat de Física, Universitat de Barcelona, Diagonal 645, 08028 Barcelona, Spain.*

Advisor: Gervasi Herranz (CSIC) / Adolf Canillas (UB)

Abstract: The aim of this project is to characterize the magnetic properties of Ce:YIG. The samples have a substrate of GGG which has a high magnetic activity that obscures the signal coming from the layer. Employing magneto optical Kerr effect technique we found two wavelengths in which the high contribution of the substrate vanishes, remaining just the one from the Ce:YIG. Studying the ellipticity around those two wavelengths different conclusions can be reached. Representing the growth conditions of the samples with the magnetic parameters, it is deduced that the easy axis of the Ce:YIG is located in the crystal orientation (111). The dependance on the wavelength of the anisotropy field is an unexpected result that has been obtained. This can be explained if the loop is as a superposition of the sublattices of Fe and Ce, which have different dependences on the wavelength. Further work will be necessary.

I. INTRODUCTION

Yttrium iron garnet, as known as YIG, is a ferromagnetic material whose chemical composition is $Y_3Fe_2(FeO_4)_3$ and presents an important Faraday rotation and a good transmittance in near infra-red [1].

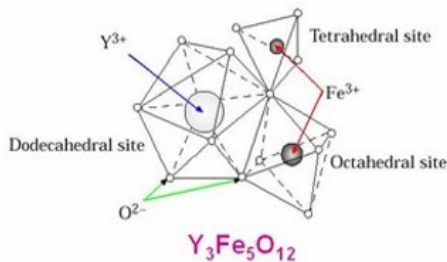


FIG. 1: Yttrium iron garnet crystal structure

Cerium doped YIG is a variant of the conventional YIG in which a part of the $(Y)^{3+}$ atoms have been replaced by $(Ce)^{3+}$ atoms. The Ce doping enables us the possibility to enhance the magneto-optical properties of the material. The doping with cerium involves the introduction of levels $4f$ in the electronic structure of the material. Thus, new states contribute to the magneto optic activity, which is highly dependent on the electronic configuration [2],[3].

The samples used in this work are made of Ce:YIG deposited on a gadolinium gallium garnet (GGG) substrate and have been synthesized by Pulsed Laser Deposition (PLD) at a $10Hz$ frequency [4]. At the table I the growth conditions of the samples under study can be seen.

Name	GGG plain	Temperature ($^{\circ}C$)	Pressure (mBar)
A1403061	(001)	800	0.3
A1403071		775	0.4
A1403101		750	0.6
A1403062	(111)	800	0.3
A1403072		775	0.4
A1403102		750	0.6

TABLE I: Samples used and its growth conditions

Due to the strong paramagnetic signal of the GGG substrate, the Ce:YIG layer is masked, making it difficult to characterize the material. With conventional characterization techniques such as SQUID the Ce:YIG signal can't be discerned.

Magneto optical Kerr effect is a way to avoid the problems originated by the high magnetic contribution of the substrate when characterizing the material. That's because in magneto optical Kerr effect the signal is strongly dependent on the light's wavelength. This allows, in particular, to choose a wavelength for which the magneto-optic activity is null for the substrate, whereas for the YIG film this activity signal is non zero. Therefore, with this wavelength-sensitivity one can only probe the magnetic properties of YIG without any contribution from the GGG substrate.

In the following, the fundamentals of magneto optical Kerr effect will be briefly discussed.

II. MAGNETO OPTICAL KERR EFFECT

The Magneto Optical Kerr Effect (MOKE) is an experimental technique used to characterize the magnetism of materials. It describes the changes on the polarization of the light once it has been reflected from a magnetic surface. Depending on the orientation of the magnetization vector \vec{M} relative to the plane of incidence of the light beam and to the surface of the material, we

*Electronic address: mespinse8@alumnes.ub.edu

can distinguish three types of MOKE: polar, longitudinal and transverse [5]. The one that concerns us here is polar, in which there is normal incidence of the light and the magnetization vector lies perpendicular to the sample surface. The influence of magnetization in this effect is a rotation (θ) of the plane of polarization and the appearance of ellipticity (ε) of the reflected linearly polarized light. See figure 2.

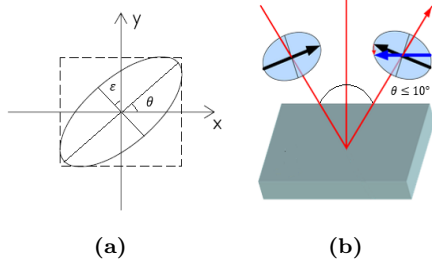


FIG. 2: a) Polarization ellipse and b) polar magneto optical Kerr effect.

III. EXPERIMENTAL SETUP

A sample of material can be described by its reflection matrix as follows

$$\begin{pmatrix} r_{ss} & r_{ps} \\ r_{sp} & r_{pp} \end{pmatrix}, \quad (1)$$

where the coefficients r_{ij} are Fresnel reflection coefficients and are defined as ratios between reflected and incident electromagnetic waves.

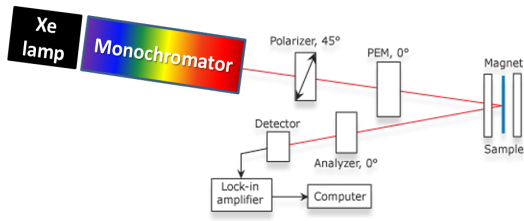


FIG. 3: Experimental setup

The experimental setup employed, described according to the light's path, consist of the following parts (see figure 3):

1. Xenon lamp.
2. Monochromator.
3. Polarizer at 45° .
4. Photoelastic modulator (PEM), which is a slab of quartz with a given optical axis, in this case at 0° . The light in this direction and its perpendicular have different velocities when passing through the material. Their outcome have a phase difference between the components, called retardation

φ . Thus, the light is modulated with a frequency, which will be essential for the identification of the signal in the Lock-in Amplifier.

5. The sample of the material under study surrounded by an electromagnet with fields up to 2 Tesla.
6. Analyser at 0° .
7. Detector

The measurements obtained go to a Lock-in Amplifier that can discern among first and second harmonic, which translates to rotation or ellipticity of the reflected light. Finally, the data goes to the computer, ready to be processed. The procedure described above can be observed in Figure 3.

Light incident to the analyzer is described using the Jones matrix formalism

$$\begin{aligned} J &= \begin{pmatrix} E_{o,x} \\ E_{o,y} \end{pmatrix} \\ &= \begin{pmatrix} r_{ss} & r_{ps} \\ r_{sp} & r_{pp} \end{pmatrix} \begin{pmatrix} e^{i\varphi/2} & 0 \\ 0 & e^{-i\varphi/2} \end{pmatrix} \begin{pmatrix} \cos 45^\circ \\ \sin 45^\circ \end{pmatrix} \quad (2) \\ &= \frac{1}{\sqrt{2}} \begin{pmatrix} r_{ss}e^{i\varphi/2} + r_{ps}e^{-i\varphi/2} \\ r_{sp}e^{i\varphi/2} + r_{pp}e^{-i\varphi/2} \end{pmatrix}, \end{aligned}$$

where linear optical elements are represented by Jones matrices. In the case above, the Jones vector of the light incident to the analyzer is equal to the Jones matrices representing the light reflected in the sample (see figure 4), the PEM and the polarizer.

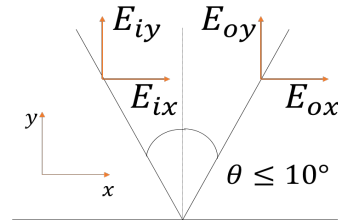


FIG. 4: Incidence and outcome of the light in a XY plane

The light's intensity on the detector can be obtained using $I_{s,p} = J_{x,y} J_{x,y}^*$. Thus, we can obtain the Intensity for the Analyzer at 0° and 90° , I_s and I_p respectively.

$$\begin{aligned} I_s &= \frac{1}{2} |r_{ss}|^2 \left[1 + \left(\frac{r_{ps}^*}{r_{ss}^*} e^{i\varphi} + \frac{r_{ps}}{r_{ss}} e^{-i\varphi} \right) \right] \\ &\approx \frac{1}{2} |r_{ss}|^2 [1 + 2\theta'_{K_s} \cos\varphi + 2\varepsilon'_{K_s} \sin\varphi] \quad (3) \end{aligned}$$

$$\begin{aligned} I_p &= \frac{1}{2} |r_{pp}|^2 \left[1 + \left(\frac{r_{sp}^*}{r_{pp}^*} e^{-i\varphi} + \frac{r_{sp}}{r_{pp}} e^{i\varphi} \right) \right] \\ &\approx \frac{1}{2} |r_{pp}|^2 [1 - 2\theta'_{K_p} \cos\varphi + 2\varepsilon'_{K_p} \sin\varphi], \quad (4) \end{aligned}$$

where we define the new variables as $\theta'_{Ks} + i\varepsilon'_{Ks} = \frac{r_{ps}}{r_{ss}}$ and $\theta'_{Kp} + i\varepsilon'_{Kp} = -\frac{r_{sp}}{r_{pp}}$, which correspond to rotation (θ) and ellipticity (φ). The quadratic term was neglected.

Having in mind that the oscillating function corresponding to the retardation angle introduced by the PEM is time dependent, we can write the $\sin\varphi$ and $\cos\varphi$ in the equations (3) and (4) in terms of the Bessel functions of first kind. Thus, considering just the first and second harmonic components, the detected intensities I_s and I_p are

$$\begin{aligned} I_s &= I_{0,s} + I_{\omega,s} + I_{2\omega,s} \\ &= \frac{1}{2} |r_{ss}|^2 [1 + 2J_0(\varphi_0)\theta'_{Ks} + 4J_1(\varphi_0)\varepsilon'_{Ks}\sin\omega t \\ &\quad + 4J_2(\varphi_0)\theta'_{Ks}\cos 2\omega t], \end{aligned} \quad (5)$$

$$\begin{aligned} I_p &= I_{0,p} + I_{\omega,p} + I_{2\omega,p} \\ &= \frac{1}{2} |r_{pp}|^2 [1 - 2J_0(\varphi_0)\theta'_{Kp} - 4J_1(\varphi_0)\varepsilon'_{Kp}\sin\omega t \\ &\quad + 4J_2(\varphi_0)\theta'_{Kp}\cos 2\omega t]. \end{aligned} \quad (6)$$

To proceed, the amplitude of PEM retardation angle φ_0 can be set in order to cancel $J_0(\varphi_0)$. Thus, setting the angle equal to $\varphi_0 = 137.8^\circ$, the component I_0 of the intensity becomes independent on θ_k . Now, the Kerr rotation and ellipticity can be obtained by

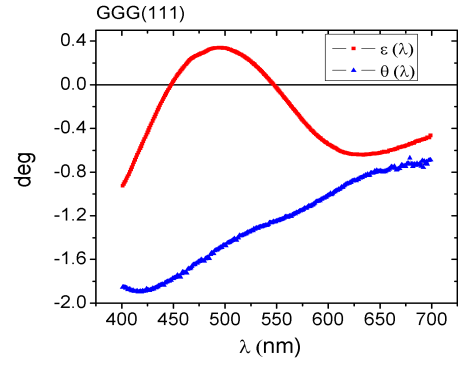
$$\begin{aligned} \theta'_{Ks} &= \frac{1}{4k} \frac{1}{J_2(\varphi_0)} \frac{I_{2\omega,s}}{I_{0,s}}, & \varepsilon'_{Ks} &= \frac{1}{4k} \frac{1}{J_1(\varphi_0)} \frac{I_{\omega,s}}{I_{0,s}}, \\ \theta'_{Kp} &= -\frac{1}{4k} \frac{1}{J_2(\varphi_0)} \frac{I_{2\omega,p}}{I_{0,p}}, & \varepsilon'_{Kp} &= \frac{1}{4k} \frac{1}{J_1(\varphi_0)} \frac{I_{\omega,p}}{I_{0,p}}, \end{aligned}$$

where the constant k can be obtained by calibration and $I_0 = I_{dc}$ [6].

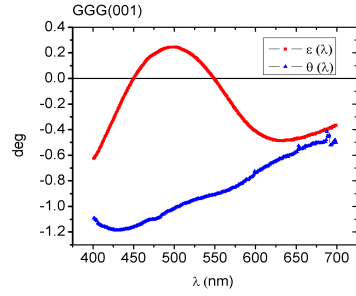
IV. RESULTS

The figure 5 represents the rotation and ellipticity spectra at visible wavelengths for two GGG substrates with different crystal orientations.

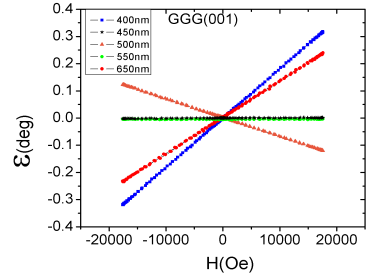
As expected, the spectra of both Ce:YIG (001), figure 5b, and (111), figure 5a, are very similar. Notice that in both cases the rotation spectra does not cross the zero but the ellipticity does it twice. Because we are interested in finding the wavelengths in which the signal of the substrate is minimal and thus observe the weaker signal coming from the layer, from now on the parameter employed will be only ellipticity. In the GGG(001) case and for a concrete number of wavelengths, the ellipticity in function of the applied magnetic field has been represented, figure 5c. It is easy to see that ellipticity vanishes in the $\lambda \sim 450nm$ and



(a)



(b)



(c)

FIG. 5: Kerr rotation and ellipticity of substrates a) GGG(111) and b) GGG(001) at visible spectra at $H = -20kOe$; c) wavelengths at which ε vanishes.

$\lambda \sim 550nm$ cases. Hence, it is demonstrated that there are two wavelengths in which the contribution of the substrate is null.

The figure 6 illustrates the ellipticity's dependence on the magnetic field for different wavelengths around the two zeros above mentioned in a Ce:YIG sample. Studying the variation of the ellipticity in a magnetic field cycle for different wavelengths around the two zeros, different conclusions can be reached. The main finding is that the slope of the substrate's contribution changes its sign. This phenomenon can be observed in both figures for high fields, specially in figure 6b, where the variation of the slope is substantially higher. This behaviour was expected, as we saw in figure 5c.

Similarly, a reversal in the loop's slope can be observed in figure 6a, while in the figure 6b it remains the same. This procedure has been repeated for all the samples with different growth conditions and crystal orientations and in all cases the result is the same.

As a next step, we could look for a correlation among the growth conditions, the saturation ellipticity, ε_{sat} , and the saturation magnetic field, H_{sat} . The saturation parameters can be extracted from the previous figures, the hysteresis loops. Choosing a concrete loop, two straight lines can be adjusted for the ranges at high and low magnetic field, as the figure 7 shows. The intersection point between these two lines corresponds to the ε_{sat} and H_{sat} .

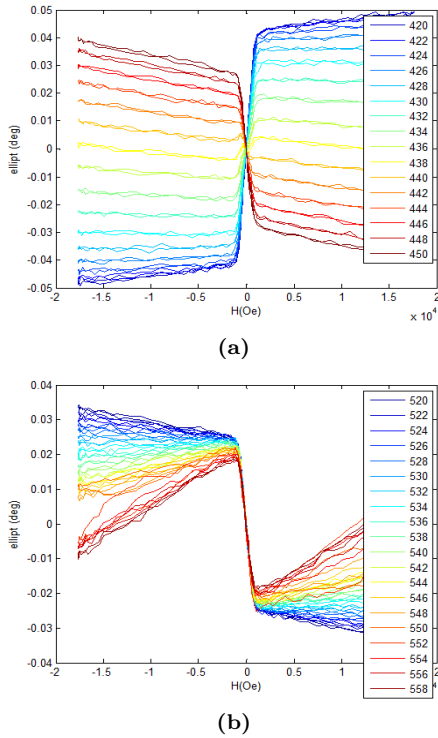


FIG. 6: Ellipticity's dependence on applied magnetic field for the sample A1403062 around a) the first zero $\lambda \sim 450nm$ and b) second zero $\lambda \sim 550nm$.

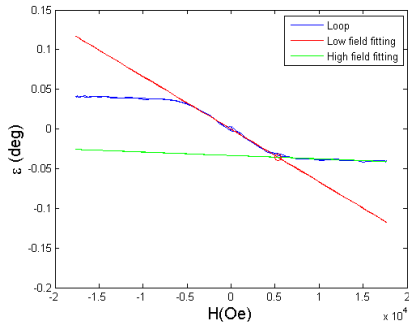


FIG. 7: Fitting at high and low field for a hysteresis loop at $\lambda = 450nm$. The intersection point corresponds to the values H_{sat} and E_{sat} .

Notice that at high fields the loop is not constant in the ellipticity value; it has a slight slope. We checked with this method that the slope doesn't affect the saturation value obtained by doing the fitting of the figure 7. From now on H_{sat} would be called apparent H_a .

Representing the ϵ_{sat} and H_a values as a function of the oxygen pressure at which the samples were grown, the figure 8 is obtained.

From the illustration 8 it could be pointed out that there's no clear correlation between the growth conditions and the saturation values. However, an important conclusion can be deduced from the figure 8b: the easy

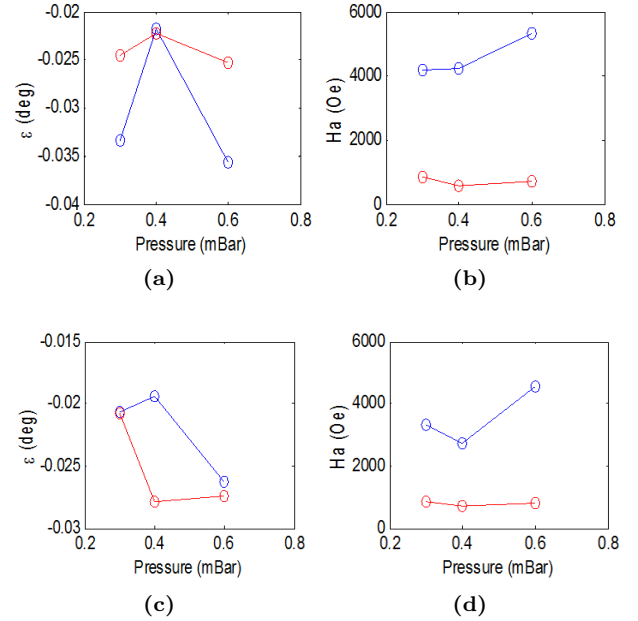


FIG. 8: ϵ_{sat} and H_a values as a function of oxygen pressure at a), b) $\lambda = 450nm$ and c), d) $\lambda = 550nm$ for the six different samples at table I. In blue, the ones with cristal orientation (001) and red the ones with (111).

axis of the Ce:YIG is (111). The applied magnetic field at which the Ce:YIG (111) saturates is clearly inferior to that of Ce:YIG (001).

The same procedure has been made for the samples at $\lambda = 550nm$, with a similar result, as the figure 8d illustrates. It could be observed again that the easy axis is in the (111) orientation with an approximated value of $H_a \sim 900Oe$.

The differences in the H_a at different oxygen pressures (figures 8b, 8d) it's due to the change in the stequiometric value of the oxygens when the pressure is changed. This variation of oxygen changes the valence of $(Fe)^{3+}$ and $(Ce)^{4+}$ and that implies a variation of the magnetization. Thus, the anisotropy's shape, which has a strong dependance on magnetization, varies, leading at different values of the H_a for different pressures.

Notice that the saturation magnetic field value should not depend on the wavelength, due to its intrinsic behaviour, but it does in the illustrations 8b and 8d, even when the growth conditions remain the same. That's an unexpected outcome that can be explained if we take into account that the hysteresis loop of the Ce:YIG material is really the superposition of two loops that are the contributions of Ce and Fe sublattices (see figure 9). Since each one of them has different dependance on the wavelength, the variation in the H_a value for distinct wavelengths is explained. This has been rigorously studied. For further detail see [7].

The figures 8a and 8c illustrate the ϵ_{sat} value as a function of the oxygen pressure. If we take into account that the relative variation of the values in the y-axis is

small, we could consider the value of ε_{sat} constant for different pressures.

Figure 8 has been repeated for temperature as a growth parameter instead of pressure, achieving similar results.

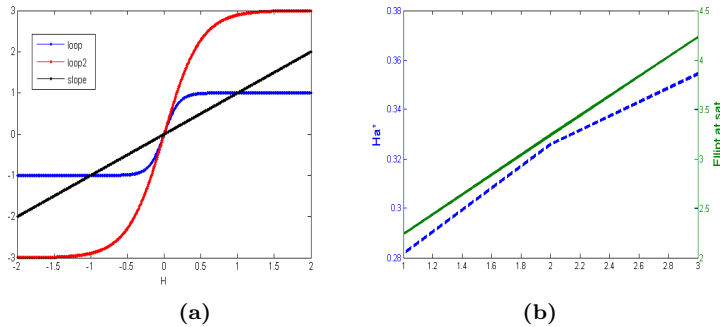


FIG. 9: a) Two loops + slope model for a hysteresis loop. Changing the amplitude of loop2, the H_a varies with it as figure b) shows. b) Change of H_a with the amplitude of loop2.

To summarise the properties of the sample's material, we carried out a comparison between the two different crystal orientation of the Ce:YIG and a third YIG sample without doping. The figure 10 presents the results at the same wavelength $\lambda = 450nm$ and same pressure.

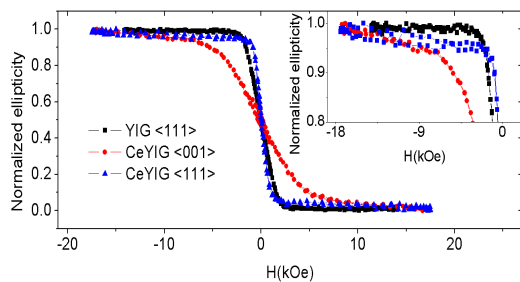


FIG. 10: YIG(111), Ce:YIG(111) and Ce:YIG(001) comparison at $\lambda = 450nm$

The figure above shows that the saturation field for the

sample Ce:YIG (111) is lower than the doped sample with cristal orientation (001). Therefore, this is another visual demonstration that the easy axis of Ce:YIG is found in the (111) orientation.

Additionally, on the non-doped sample it can be observed that the saturation field doesn't depend on the wavelength, as we expected.

V. CONCLUSIONS

Of this study it can be drawn that magneto optical Kerr effect is the appropriate technique to characterize materials such as the one in study, Ce:YIG/GGG, as it achieves what other experimental techniques can't.

By employing MOKE on two samples of different crystal orientations of YIG doped with cerium, we can conclude that the easy axis of this material is located on the (111) crystal orientation, since its saturation field is the lowest found. That has been ratified separately in two different graphs representing H_a as a function of the pressure and by comparing the two samples of Ce:YIG (001) and (111).

The H_a represented in figures 8b and 8d it's not a property of the material, inasmuch as it depends on the wavelength.

Our approach to explain the dependance on the wavelength of the saturation field is that the hysteresis loop it's the sum of two loops stemming from the contributions of iron and cerium sublattices.

Acknowledgments

I would like to express my deep gratitude to Blai Casals for his patient guidance and valuable help; to Dr. Gervasi Herranz for his advice and assistance and to Dr. Adolf Canillas. My grateful thanks are also extended to Sara Martí for letting me know about ICMAB, my university colleagues for their understanding and my partner for his continuous support.

-
- [1] Gomi, Manabu et al. *Giant Faraday rotation of Ce-Substituted YIG films epitaxially grown by RF sputtering*, Japanese Journal of Applied Physics 27.8A(1988):L1536.
 - [2] Xu, You et al. *A theoretical investigation on the strong magneto-optical enhancement in Ce-substituted yttrium iron garnet*, Journal of Physics: Condensed Matter 5.47(1994):8927.
 - [3] Guo, Xiaofeng et al. *Cerium Substitution in Yttrium Iron Garnet: Valence State, Structure, and Energetics*, Chemistry of Materials 26.2(2014):1133.
 - [4] Rubio, Carlos (2014) *Characterization of Ce:YIG epitaxial thin films*, Final Degree Project, UAB.
 - [5] Zvezdin, A.K. and Kotov, V.A, *Modern Magnetooptics and magneto-optical materials*, (Institute of Physics Publishing, London, 1997, 1st. ed).
 - [6] Vlasin, Ondrej (2014) *Magneto-optical confocal microscopy of magnetic nanostructures*, Ph.D. Thesis. UAB: Spain
 - [7] Casals, B., Espínola, M. et al. Paper in preparation.
 - [8] Calcedo Roque, Jose Manuel (2012) *Magneto-optical spectroscopy of complex systems: magnetic oxides and photonic crystals*, Ph.D. Thesis. UAB: Spain